Nondestructive testing of additively manufactured material based on ultrasonic scattering measurement

Yongfeng Song[a], Xuhui Zi[b], Yingdong Fu[a], Xiongbing Li[a,*], Chao Chen[b,*], Kechao Zhou[b]

[a] *School of Traffic and Transportation Engineering, Central South University, Changsha 410075, China*
[b] *State Key Laboratory of Powder Metallurgy, Central South University, Changsha 410083, China*

ABSTRACT

To improve ultrasonic testing capability for additively manufactured materials, extreme value statistics is employed to calculate the experimental confidence bounds of structural noise, which can be treated as time-dependent thresholds for ultrasonic C-scan image segmentation. A 316L stainless steel sample manufactured by selective laser melting is used for ultrasonic scattering measurements with a focused transducer. Compared with the fixed threshold used in the traditional C-scan image segmentation, the time-dependent threshold can effectively distinguish the flaw echoes from the background of structural noise. The optical microscopy measurement results show that the present method can avoid both missed detections and false positives.

1. Introduction

Additively manufactured (AM) parts can be produced by selective laser melting (SLM) process with mechanical properties comparable to those of conventional cast parts [1]. However, the macroscopic flaws (e.g. isolated pores, cracks, and lacks of fusion) can destroy the mechanical properties of SLM additively manufactured metallic material [2]. To comply with the high safety standards, quality assurance is pursued using ultrasonic inspection. Rieder et al. [1] and Lévesque et al. [3] have presented online inspection methods for AM materials using contact transducer underneath the build-platform and non-contact laser ultrasonics, respectively. The offline inspection methods are also developed with phased array [1] and conventional C-scan approach [2]. However, the ultrasonic inspection for AM materials is still a challenge because flaws will go undetected when the reflected echoes from the flaws are hidden by undesirable structural noise in ultrasonic waveforms.

The structural noise is known as the ultrasonic backscattering signal, which is constituted by coherent scattering waves travelling back to the transducer in the opposite direction of the incident ultrasonic wave [4]. The scattering of ultrasonic wave is caused by acoustic impedance differences existing within the propagation medium, which has a significant detrimental effect on nondestructive testing applications [5]. Due to the need to achieve better testing quality, the ultrasonic structural noise has been an active research topic for the past decade [6]. Moreover, the fact that the ultrasonic backscattering signal carries important information on the geometric and elastic properties of

the material microstructure, which leads to intensified interest in ultrasonic scattering measurements and modeling [7].

If there are no porosity and nonmetallic phase in the propagation medium, the structural noise can be also recognized as the grain noise. The first realistic model of grain noise was developed by Rose [8]. Han and Thompson [9] extended Rose's work to the scattering in hexagonal polycrystalline materials with duplex microstructures. The grain noise model for polycrystals with arbitrary crystallite and macroscopic texture symmetries was developed by Li and Rokhlin [7]. However, all of these works are in frequency domain, which can be used in material characterization but are hardly applicable to flaw detection. Recently, Ghoshal and Turner [10] have developed a time-dependent grain noise model called singly-scattered response (SSR) model, which produces equivalent results and behaviors as the model in the frequency domain. The theoretical SSR model assumes that the ultrasonic waves scatter only once from the microstructure, and includes the three parts: experimental calibration, backscatter coefficient, and the transducer beam pattern [10].

More recently, Song et al. [11] developed a forward backscattering model to estimate the upper bound of grain noise based on the SSR model [10,12] and extreme value theory [13]. The upper bound can be regarded as the time-dependent threshold in ultrasonic inspection and used to locate the flaws automatically; however, the previous SSR model [12] is not applicable for the strongly-scattering stainless steel alloy fabricated by SLM, whose structural noises are attributed to not only the columnar grain, but also the inherent porosity, texture and residual stress. Additionally, the effect of grain noise's non-zero spatial

---

* Corresponding author.
E-mail addresses: lixb213@csu.edu.cn (X. Li), pkhqchenchao@csu.edu.cn (C. Chen).

average on the theoretical bound is ignored [11].

In this work, we highlight the experimental bounds of structural noise from SLM stainless steel, in which the ultrasonic waves are considered multiple scattering. A predictor-corrector algorithm for measuring the experimental bounds is given in terms of the extreme value statistics; both the spatial standard deviation and spatial average of structural noise are taken into consideration. Finally, the experimental bounds are used in ultrasonic inspection, and the present method is verified with a 316L stainless steel sample fabricated by SLM.

2. Method

When the ensemble was obtained by collecting waveforms at different spatial locations on the sample, the spatial average and standard deviation of an ensemble of collected ultrasonic waveforms are [14].

$$\mu^{\exp}(t) = \frac{1}{N} \sum_{i=1}^{N} V_i(t), \tag{1}$$

$$\sigma^{\exp}(t) = \sqrt{\frac{1}{N} \sum_{i=1}^{N} V_i^2(t) - \left(\frac{1}{N} \sum_{i=1}^{N} V_i(t)\right)^2}, \tag{2}$$

where i denotes the i-th waveform in the ensemble containing a total of N normally distributed waveforms and $V_i(t)$ is the time-dependent amplitude (typically a voltage) of the i-th waveform. The spatial average and standard deviation at time t refer to the concentration and dispersion of backscattering data from different lateral transducer positions, and they are denoted by the superscript exp to emphasize that they are experimentally measureable parameters. Notice that $V_i(t)$ are assumed to be distributed in a Gaussian manner at all depths, even in the focal zone [15].

Based on the fundamental assumption that $V_i(t)$ belongs to a normal distribution, the extreme value statistics [13] can be introduced to describe the relationship between the maximum/minimum amplitudes in the ensemble $A_{\max}^{\exp}(t) = \max\{V_i(t)\}$ or $A_{\min}^{\exp}(t) = \min\{V_i(t)\}$, spatial average $\mu^{\exp}(t)$ and spatial standard deviation $\sigma^{\exp}(t)$. More strong assumptions are used here: (1) the polycrystalline materials should be strictly statistically homogeneous; (2) there are no vertical offsets to the baseline signal; (3) the effects of measurement system (e.g. electromagnetic interference, averaging time, scanning speed, etc.) can be neglected; (4) the separation between two consecutive transducer positions should be large enough that the two backscattered signals are fully uncorrelated. All of these assumptions are used to ensure that all the waveforms are independent and identically distributed (IID).

Assuming that $V_i(t)$ are normally distributed and that $A_{\max}^{\exp}(t)$ and $A_{\min}^{\exp}(t)$ obey the Gumbel distribution, then, taking advantage of the useful properties of the Gumbel distribution, the upper bound of $A_{\max}^{\exp}(t)$ and the lower bound of $A_{\min}^{\exp}(t)$ can be given as:

$$U^{\exp}(t) = b_N^{\max}(t) - a_N^{\max}(t)\ln[-\ln((1+\alpha)/2)],$$
$$L^{\exp}(t) = -b_N^{\min}(t) + a_N^{\min}(t)\ln[-\ln((1+\alpha)/2)], \tag{3}$$

where α is the confidence level. The normalization constants $a_N^{\max}(t)$, $a_N^{\min}(t)$, $b_N^{\max}(t)$ and $b_N^{\min}(t)$ can be defined as [13]:

$$a_N^{\max}(t) = a_N^{\min}(t) = \frac{\sigma^{\exp}(t)}{\sqrt{2\ln N}},$$
$$b_N^{\max}(t) = \left[\sqrt{2\ln N} - \frac{\ln\ln N + \ln 4\pi}{2\sqrt{2\ln N}}\right]\sigma^{\exp}(t) + \mu^{\exp}(t),$$
$$b_N^{\min}(t) = \left[\sqrt{2\ln N} - \frac{\ln\ln N + \ln 4\pi}{2\sqrt{2\ln N}}\right]\sigma^{\exp}(t) - \mu^{\exp}(t), \tag{4}$$

where $\mu^{\exp}(t)$ and $\sigma^{\exp}(t)$ are the time-dependent spatial average and standard deviation curve, and N denotes the number of waveform. In practice, the bounds of structural noise can be used to establish amplitude thresholds to be triggered by a flaw echo. Therefore, Eq. (3) is the primary result of this article.

To reduce the error of the bounds, an ideal reference sample

without any flaws is required, but this is unrealistic in practice. Besides, some flaws could be missed if a large scanning step is used to acquire independent backscattered signals. Thus, a predictor-corrector algorithm, or a self-referenced method, is introduced here to establish the bounds with smaller step. First, the predictor step: (1) choose a subset $V_j(t)$ from $V_i(t)$ with a large enough virtual scanning step, where $V_j(t)$ should include at least 1000 independent backscattered signals; (2) use the subset $V_j(t)$ to acquire $U^{\exp}(t)$ and $L^{\exp}(t)$. Next, the corrector step: (1) remove the waveforms $V_j(t) > U^{\exp}(t)$ or $V_j(t) < L^{\exp}(t)$ form $V_j(t)$, which might be flaws echoes; (2) get a new subset $\hat{V}_k(t)$ and use it to acquire $\hat{U}^{\exp}(t)$ and $\hat{L}^{\exp}(t)$. Finally, $\hat{U}^{\exp}(t)$ and $\hat{L}^{\exp}(t)$ can be used to identify flaw echoes in the original ensemble $V_i(t)$. Finally, the experimental bounds can be obtained even when the waveforms scattered from the flaws are used.

To verify the present method, a few numerical examples were given by the Monte Carlo simulations. In the simulations, the number of data generated randomly was n, which means the sample size of subset $V_j(t)$ is n. Assume that the number of data points from the backscattering signal in the ensemble is Mn, and the number of data points from the anomalous flaw echo signal in the ensemble will be $(1-M)n$, where $0 \leqslant M \leqslant 1$. When the scale factor $M = 1$, all data are from the backscattering signal. On the other hand, when $M = 0$, all data are from the flaw echo. The following three conditions are assumed in the simulations: the backscattering data belong to the normal distribution $N_0(0,0.1)$, one half of the anomalous flaw echo data belong to the normal distribution $N_1(-\mu_1,\sigma_1)$, and the rest of the flaw echo data belong to the normal distribution $N_2(\mu_2,\sigma_2)$. The predicted bounds and corrected bounds can be calculated with confidence levels α and $\hat{\alpha}$, respectively. As Fig. 1 shows, the quantile-quantile plots are used to show four different simulation cases. Fig. 1(a) indicates that if the amplitude of flaw echo was dramatically larger than the amplitude of backscattering signal, both the predicted bounds and corrected bounds can identify the flaw easily. The data points within the predicted bounds constitute a new subset. Because all the flaw echo data in the initial subset were removed, the corrected bounds given by the new subset can be made much narrower while maintaining the same confidence level. Fig. 1(b) shows all the flaw echo data can be identified and the simulated amplitude difference between the backscattering data and flaw echo data was only 3.15 dB (lower than the requirement of 6-dB in British Standard EN 12680-1:2003). As shown in Fig. 1(c), when the proportion of flaw echo data at time t is larger than 1%, the presented self-referenced method breaks down, because the flaws are widely distributed at one layer in the sample. Fig. 1(d) shows that the confidence level can be enhanced in the corrector step, and all the flaw echo data can still be identified when the simulated amplitude difference was 5.22 dB (also lower than 6 dB).

3. Experiments

3.1. Preparations

To illustrate the application of the proposed methodology, a 316L stainless steel sample (size 40 mm × 40 mm × 15 mm, mass 196.34 g, volumetric porosity 0.38%) fabricated by SLM was used to conduct the ultrasonic experiments. The volume fraction was measured by the Archimedes method. The sample was produced by Farsoon F271M at a laser power of 180 W; it should be noted that a lower laser power than the usual 225 W was intentionally used to produce more flaws in the specimen. The laser scanning velocity was 1000 mm/s, the hatch spacing was 0.09 mm and the layer thickness was 0.03 mm. All processing occurred in a nitrogen environment with less than 0.1% oxygen to avoid oxidation and degradation of the material during the process [16]. In the SLM process, the sample was heated tautologically by the heat transfer from the uppermost laser all the time, which leads to the residual stresses in the samples. Thus, to prevent the sample from cracking by residual stresses, stress relief annealing was conducted after
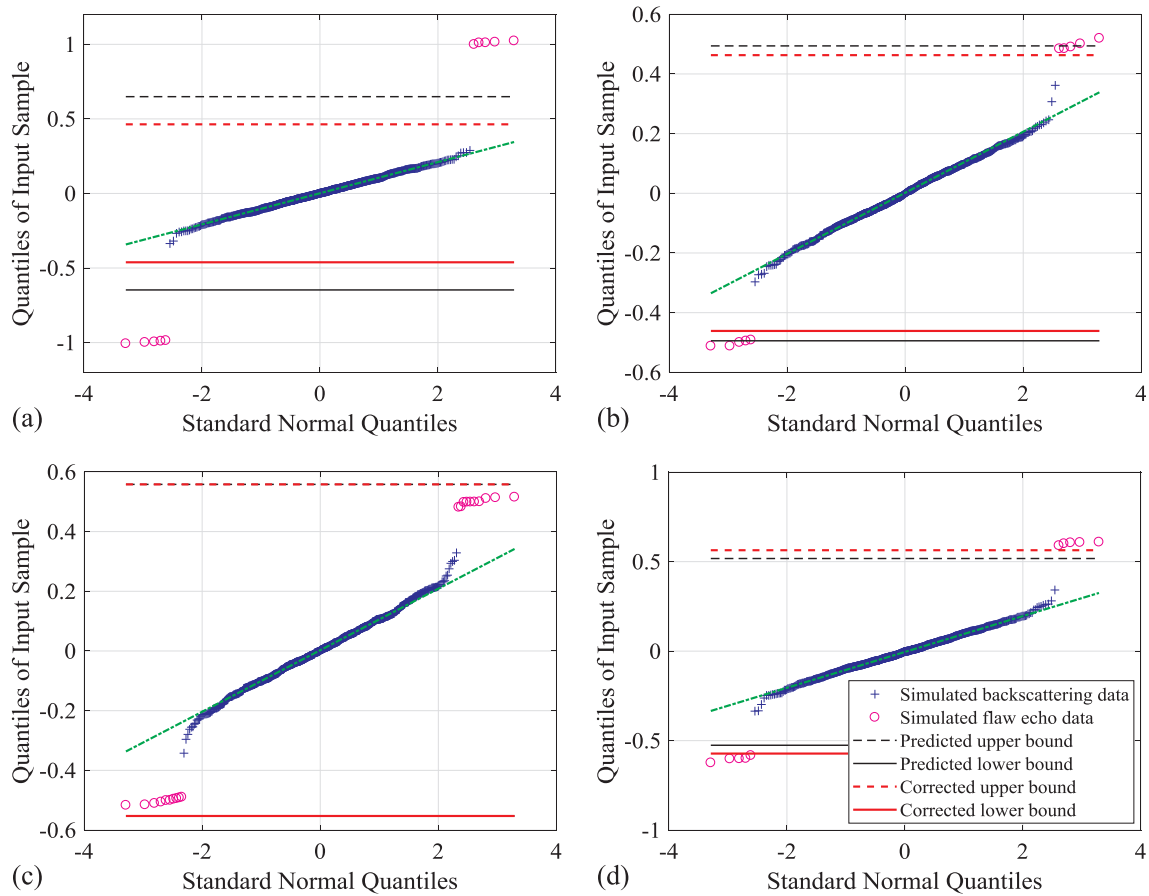
Fig. 1. Numerical examples simulated by the Monte Carlo method. (a) $M = 0.99$, $\mu_1 = \mu_2 = 1$, $\sigma_1 = \sigma_2 = 0.01$, $\alpha = \hat{\alpha} = 99\%$, (b) $M = 0.99$, $\mu_1 = \mu_2 = 0.5$, $\sigma_1 = \sigma_2 = 0.01$, $\alpha = \hat{\alpha} = 99\%$, (c) $M = 0.95$, $\mu_1 = \mu_2 = 0.5$, $\sigma_1 = \sigma_2 = 0.01$, $\alpha = \hat{\alpha} = 99\%$, (d) $M = 0.99$, $\mu_1 = \mu_2 = 0.6$, $\sigma_1 = \sigma_2 = 0.01$, $\alpha = 99\%$, $\hat{\alpha} = 99.99\%$.

the SLM process.

As shown in Fig. 2(a), a standard alternating X/Y raster scanning strategy was adopted during the SLM process, which features bidirectional hatches of a layer 'n' performed in Y-axis whilst the next layer 'n + 1' turned 67° [16]. Moreover, the laser scanning velocity, hatch spacing, and layer thickness are demonstrated in Fig. 2(a). An etchant of 20% HF + 10% HNO$_3$ + 70% H$_2$O was used to etch three cross-sections for 20 min [17], then optical micrographs (OM) were obtained by an Olympus BX53M metallographic microscope. With low magnification (100x), Fig. 2(b) shows OM images of the fabricated 316L

stainless steel sample in three mutually perpendicular planes. Regular laser melted tracks associated with the alternating 67° filling strategy are shown clearly in X-Y plane. Also, the SLM formation features of layer by layer superposition are observed in Y-Z/X-Z plane. By using the linear intercept method [17], the length and width of the columnar grains can be measured as 448.8 ± 92.7 µm and 87.6 ± 3.7 µm, while the layer thickness is measured to be 37.8 ± 4.9 µm. The grain size measurements in three directions are approximately normally distributed.

Via Fig. 2(b), not only the columnar grains, but also the micro-pores
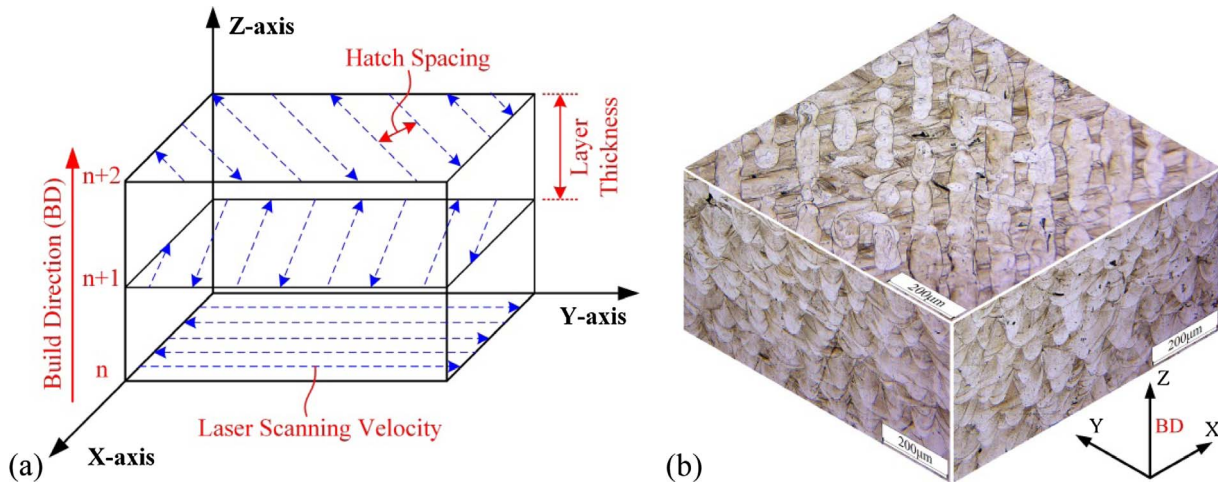
Fig. 2. The relationship between the laser scanning strategy and the microstructure of 316L stainless steel. (a) laser scanning strategy used in SLM experiments and the orientation of the built sample. (b) microstructure in three mutually perpendicular planes that depicts the typical columnar grain structures.

Angle	-80°
Length	27.1 μm
Width	6.6 μm
Area	104.8 μm²
Length-Width Ratio	4.1
Wrinkled Degree	31.6

Angle	-11°
Length	7.5 μm
Minor	6.9 μm
Area	41.1 μm²
Length-Width Ratio	1.1
Wrinkled Degree	13.1
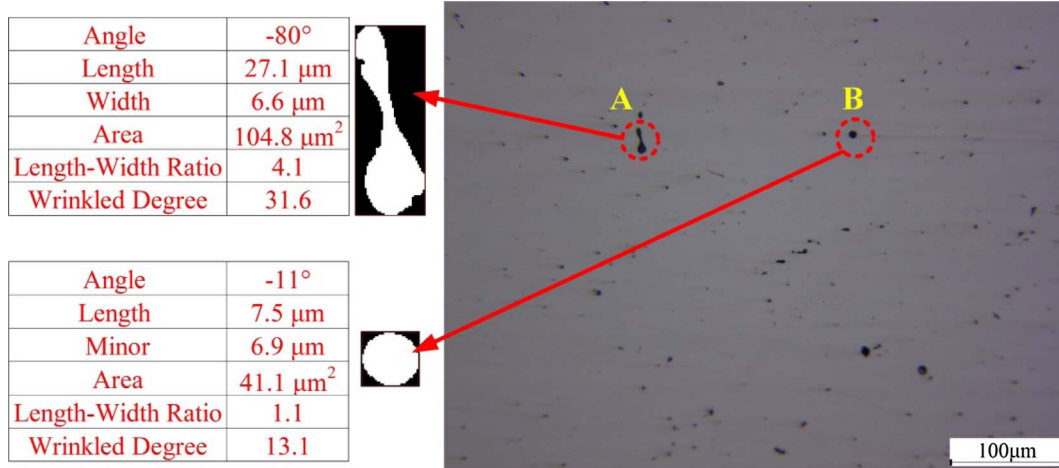
Fig. 3. A typical micrograph of micro-pores in X-Y plane. Two magnified binary images of micro-pores A and B are analyzed.

can be observed. This kind of micro-pores is distributed and attributable to the inherent nonzero porosity of the 316L stainless steel fabricated by SLM. Prior knowledge of micro-pores is necessary. Therefore, the sample was re-polished and observed over two mutually perpendicular planes X-Y and Y-Z by the microscope with higher magnification (200x). Fig. 3 shows the microstructure of micro-pores in X-Y plane. The length, width, and area of these two typical binary images of micro-pores are measured and shown in Fig. 3. The shapes of the micro-pores are characterized by two parameters, length-width ratio and wrinkled degree. The wrinkled degree is defined as the ratio of the square of perimeter and area based on the isoperimetric inequality [18]. The orientation of micro-pore is described as the angle between the preferred direction of micro-pore and the horizontal direction of the OM image. For examples, the micro-pore A is larger, longer, more wrinkled and more tilted, and the micro-pore B is more similar to a circle and more smooth.

Because the size, shape, and orientation of the micro-pores are random, the properties of micro-pores are measured and analyzed statistically. Fifty OM images of 316 stainless steel sample fabricated by SLM were individually captured in X-Y and Y-Z planes. As shown in Fig. 4(a)–(e), the distributions of the porosity characteristics in X-Y plane are non-Gaussian. The angle distribution of micro-pores in Y-Z plane is shown in Fig. 4(f). The other distributions in Y-Z plane are similar to those in X-Y plane. Additionally, the median, the lower-quartile and upper-quartile of the micro-pore properties are shown in Table 1. The median values of length and width of the micro-pores are ~4.0 μm and ~2.8 μm, and these two values are the key comparative parameters in the following macroscopical flaw detection experiments. Furthermore, most shapes of the micro-pores are relatively circular and smooth. Most orientations are parallel to horizontal direction or vertical direction of the OM image. Although the reasons for these orientation distributions are beyond the scope of this paper, the micro-pores paralleled to the horizontal direction in Y-Z plane were generally considered to be resulted from the microscopic lack of fusion of two adjacent layers of powders.

3.2. Ultrasonic measurements

As shown in Fig. 5, normal incidence pulse/echo measurement was conducted in a water immersion tank using a JSR DPR 300 pulser/receiver, a 15 MHz focused transducer (2-in. focal length, 0.5-in. element diameter), a 200 MHz DAQ card and a computer-controlled micro-positioning system. The gain of DPR 300 was set at 73 dB. The ultrasonic C-scan plane is parallel to the X-Y plane of the sample.

Material path is a key experimental parameter of immersive C-scan with a focal transducer, which is the distance between the front-wall of the sample and the focus point in the sample. To set the material path, the longitudinal wave velocities are measured in three mutually perpendicular directions using an echo overlapping algorithm [19]. The experimental velocities were 5749.5 ± 5.9 m/s, 5701.3 ± 6.2 m/s, and 5695.6 ± 5.5 m/s in directions z, x, and y, respectively. The material path was then chosen as $MP = 6$ mm, so the water path, distance from the transducer surface to the front surface of the test sample, can be calculated by

$$WP = F - \frac{c_L}{c_f}MP, \tag{5}$$

where F is the focal length, and c_f and c_L are the longitudinal wave velocities in water and in the z direction of the sample, respectively; thus, the water path was set as 27.58 mm. Moreover, the velocities in three mutually perpendicular directions also revealed the overall anisotropy of the sample. According to the analogous microstructures in Y-Z and Z-X planes as Fig. 2(b) shown, the velocities measured in directions x and y were the same. However, due to the microstructure difference, the velocity measured in z direction was relatively larger compared to the velocities in other two directions. It also indicates that the effective elasticity modulus in z direction is relatively larger, and the sample is verified to be macroscopically anisotropic.

The original ensemble $V_i(t)$ was obtained from the C-scan of the sample at different spatial locations. Within a rectangular grid of 32.5 mm × 34 mm over the sample, 111,166 (326 × 341) waveforms were recorded; the scanning step was 0.1 mm, which matched the hatch spacing of SLM. However, most of them are not independent. Thus, the predictor-corrector algorithm was used to correct the independent sampling size with a virtual scanning step and to calculate the bounds of the structural noise. The virtual scanning step should be decided with the spatial correlation coefficient (SCC) of the structure noise [6], assuming SCC ≤ 50% is acceptable. In this measurement, SCC was ~92.99% if the virtual scanning step is 0.1 mm, and ~48.14% if the virtual scanning step is 0.9 mm. Therefore, a subset $V_j(t)$ was chosen from $V_i(t)$ to agree with the IID condition that the virtual scanning step is 0.9 mm, so the number of subset $V_j(t)$ is $N = 1406$ (37 × 38). Then the predicted bounds $U^{exp}(t)$ and $L^{exp}(t)$ can be obtained, and the confidence level was set as 99.99% in the predictor step. We can see 16 flaws from Fig. 6, whose echoes satisfy the condition that $V_j(t) > U^{exp}(t)$ or $V_j(t) < L^{exp}(t)$. As the flaw echoes were removed, the rest number of new subset $\hat{V}_k(t)$ is 1390. Fig. 7 is the quantile-quantile plot of $\hat{V}_k(t = 42 \mu s)$. From Fig. 7, we can see that the quantiles of structure noise is linearly dependent on the standard normal quantiles, thus the distribution of structure noise is approximate to normal distribution, which establishes the basis that Gumbel distribution works for the material we studied. Next, $\hat{V}_k(t)$ was used to acquire the bounds
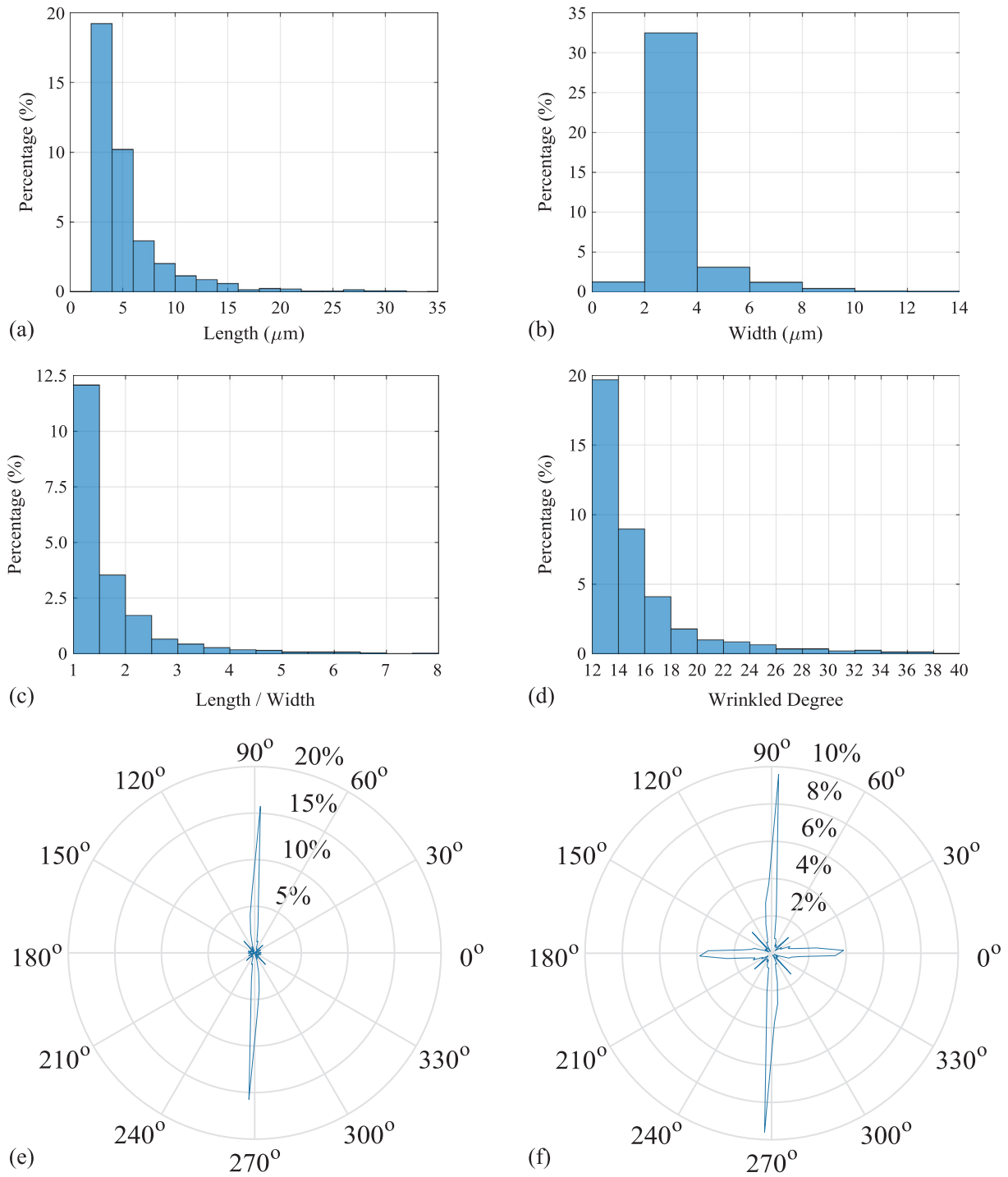
Fig. 4. The distribution diagrams of the porosity characteristics (a) length distribution in X-Y plane, (b) width distribution in X-Y plane, (c) length-width ratio distribution in X-Y plane, (d) wrinkled degree distribution in X-Y plane, (e) angle distribution in X-Y plane, (f) angle distribution in Y-Z plane.

Table 1
The overall characteristics of porosity.

Plane	Length (µm)	Width (µm)	Area (µm^2)	Length-Width Ratio	Wrinkled Degree
X-Y	3.9 (2.9, 5.8)	2.7 (2.4, 3.2)	8.7 (5.5, 14.1)	1.4 (1.1, 1.7)	13.9 (13.2, 16.2)
Y-Z	4.1 (3.0, 5.9)	2.8 (2.5, 3.3)	9.0 (5.9, 15.0)	1.3 (1.1, 1.8)	14.0 (13.2, 16.1)

(Notes: the value outside the round brackets in this table is the median value, and the values inside the round brackets are the lower-quartile and upper-quartile, respectively).
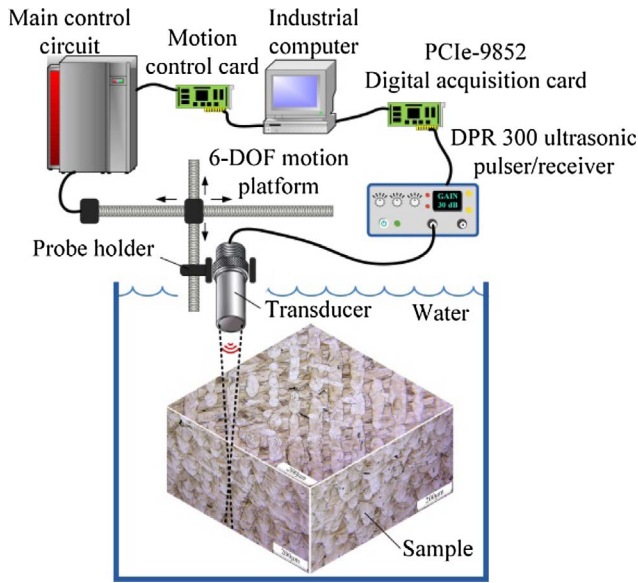
Fig. 5. The schematic of ultrasonic scattering measurement setup for pulse-echo configuration.

Fig. 7. The quantile-quantile plot of structure noise data in subset $\hat{V}_k$ at 42 μs.

$\hat{U}^{\mathrm{exp}}(t)$ and $\hat{L}^{\mathrm{exp}}(t)$, and the confidence level was chosen as 99.9999% in the corrector step.

The relationship between the maximum/minimum amplitudes of $\hat{V}_k(t)$, $\hat{U}^{\mathrm{exp}}(t)$ and $\hat{L}^{\mathrm{exp}}(t)$ is shown in Fig. 8. Because $\hat{V}_k(t)$ is totally covered by the corrected bounds within the time gate from 38 to 42 μs, it can be regarded as a clear part of the SLM sample. The theoretical upper bound $U^{\mathrm{theory}}(t)$ and lower bound $L^{\mathrm{theory}}(t)$ based on SSR [12] are also shown in Fig. 8, but these bounds are undesirable since the $A_{\max}^{\mathrm{exp}}(t)$ and $A_{\min}^{\mathrm{exp}}(t)$ cannot be included in these bounds. Moreover, Fig. 8 shows a natural structural noise and a typical flaw echo from an isolated pore (flaw No. 1 will be discussed later) distinguished by the experimental bounds. The experimental bounds were then used as time-dependent thresholds to segment the C-scan image and test flaws. As shown in Fig. 9, several flaws were detected and their depths were different.

3.3. Analysis and discussions

For comparisons, the theoretical bounds based on the SSR model in Fig. 8 are used again as time-dependent thresholds in Fig. 10(a). Fig. 10(b) and (c) shows the C-scan images segmented by fixed thresholds of 0.5 V and 1.5 V, respectively. In order to analyze and verify the effectiveness of the present method, regions No. 1 to No. 4 as shown in Figs. 9 and 10 were used for optical microscopic measurements with 200x magnification. The sample was dissected by wire cutting based on the time of flights of the flaw echoes. The cubes were

then polished and examined. As shown in Fig. 11, the size of flaws in regions No. 1, No. 2, and No. 3 were about φ 88 μm, 464 × 93 μm and 156 × 66 μm, respectively. Comparing the flaw size, the columnar grain size and the micro-pore size, we can see that the detectable flaw size is smaller than the grain size but much larger than the micro-pore size. Flaw No. 3 with an irregular shape is a lack of fusion, which was induced by the insufficient melting of the powder particles [20]. The as-formed molten pool size is small at low laser energy density, thus limiting the contact area between the molten pool and the powder particles and leading to the irregular pores of No. 1 and No. 2. Now we can see that, flaw No. 1 is missed in Fig. 10(c) with the traditional fixed threshold method, and that region No. 4 is a false positive in Fig. 10(a) and 10(b) since no flaw actually exits there.

Since the noise is very bad in Fig. 10(d); the time-dependent thresholds with the SSR model do not work and the segmented image looked the same as the raw C-scan image without segmentation. One possible reason for this result is that the SSR model breaks down and underestimates the backscattering amplitude from polycrystalline metals with porosity and texture. In addition, as a sample fabricated by SLM without artificial flaws inside, we can never know the optimal fixed threshold. If the fixed threshold is not high enough, the structural noise will be dominant and this leads to the false positives as in the case of region No. 4. If the fixed threshold is too high, the flaws are usually missed as in the case of flaw No. 1.

Although the present method has been shown to improve the inspection capability for the SLM materials, it has the following limitations: (1) statistical homogeneity of the materials is required; (2) measured backscattering data are not exactly normally distributed, so a higher confidence level is necessary; (3) the effects of confidence level and virtual scanning step on the inspection results are unknown; (4) the experimental bounds are not applicable for parts with complex curved
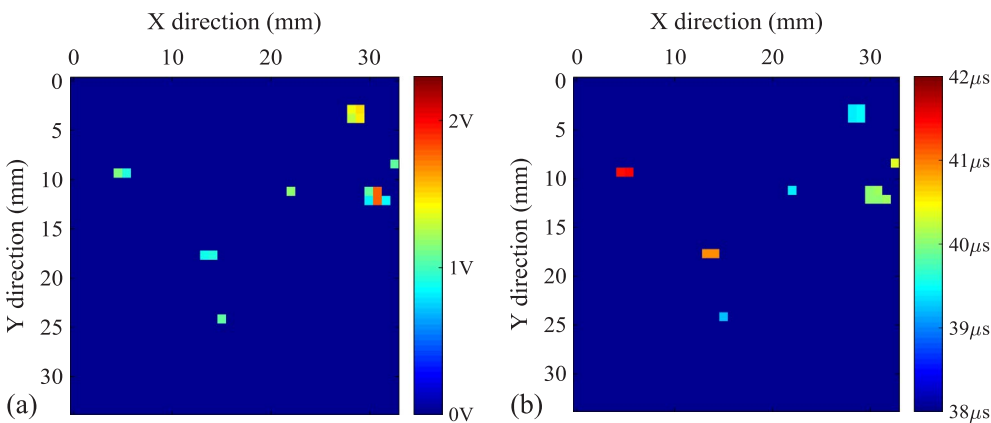
Fig. 6. The ultrasonic C-scan images of the virtual scanning subset $V_j(t)$ segmented by the predicted bounds (a) image of amplitude (b) image of time-of-flight.
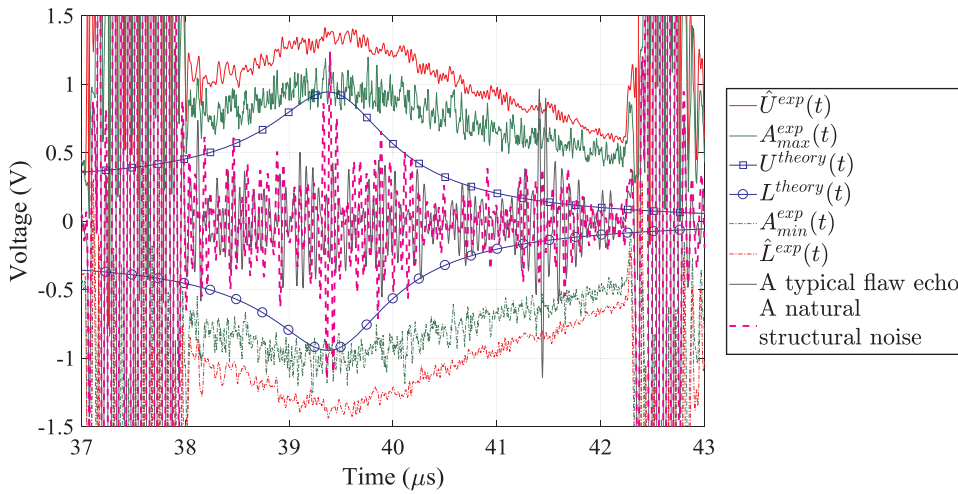
Fig. 8. The relationship between the experimental bounds, the maximum/minimum amplitudes, a natural structural noise and a typical flaw echo from an isolated pore. The theoretical bounds are based on SSR model. The confidence levels of the bounds are 99.9999%.
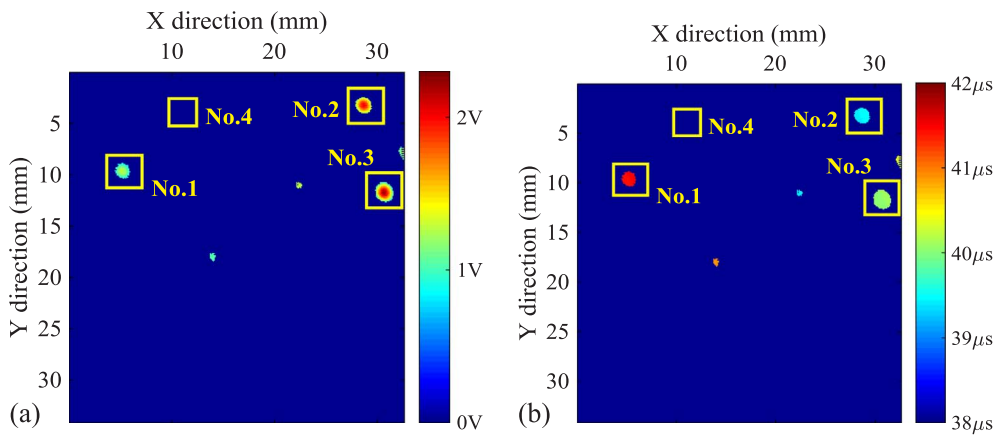
Fig. 9. The ultrasonic C-scan images segmented by the present method (a) image of amplitude, (b) image of time-of-flight. In these two images, the non-zero value represents a segmented pixel.

surface because the spatial average and standard deviation cannot be obtained, and a multiple scattering response model for AM materials is needed in order to give the theoretical bounds for parts with complex curved surface; (5) the present method is not applicable to testing distributed flaws like porosity. Further research should be focused on ultrasonic evaluation of porosity in additively manufactured materials, and the ultrasonic velocity and attenuation methods have shown their potential in evaluating porosity [21]. These are some of our current efforts and will be addressed elsewhere.

4. Summary

In this work, the ultrasonic backscattering data induced by microstructure in additively manufactured material were measured using extreme value statistics. The experimental maximum/minimum amplitudes of collected waveforms are directly related to the spatial average and standard deviation of those waveforms in the extreme value theory. Then, a predictor-corrector algorithm was introduced to derive the experimental confidence bounds on the maximum/minimum amplitudes without the need for a reference sample. The most important application of the present method is to inspect the flaws inside the additively manufactured samples under high gain. The
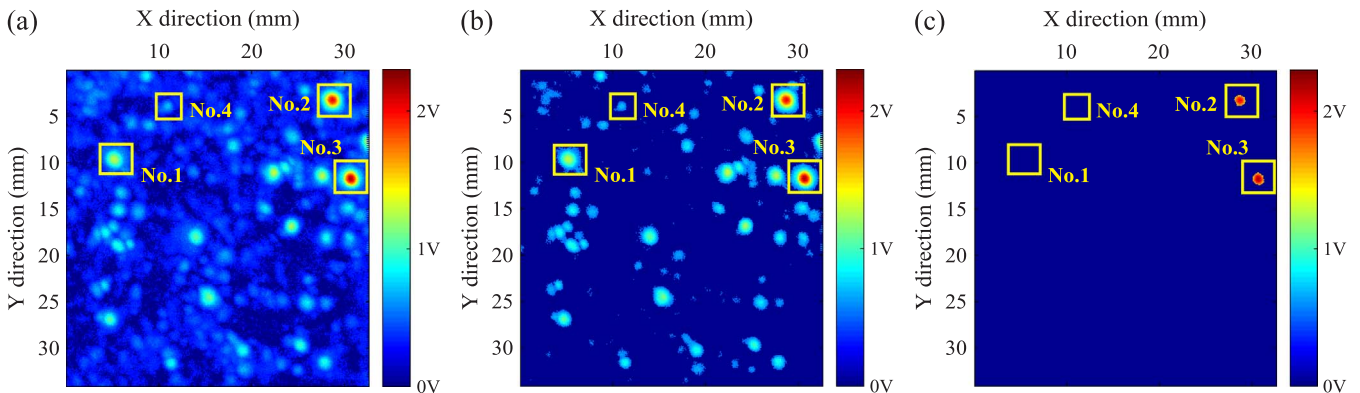
Fig. 10. The ultrasonic C-scan images segmented by different methods. (a) time-dependent thresholds with SSR model, (b) fixed threshold of 0.5 V, (c) fixed threshold of 1.5 V. In these images, the non-zero value represents a segmented pixel.
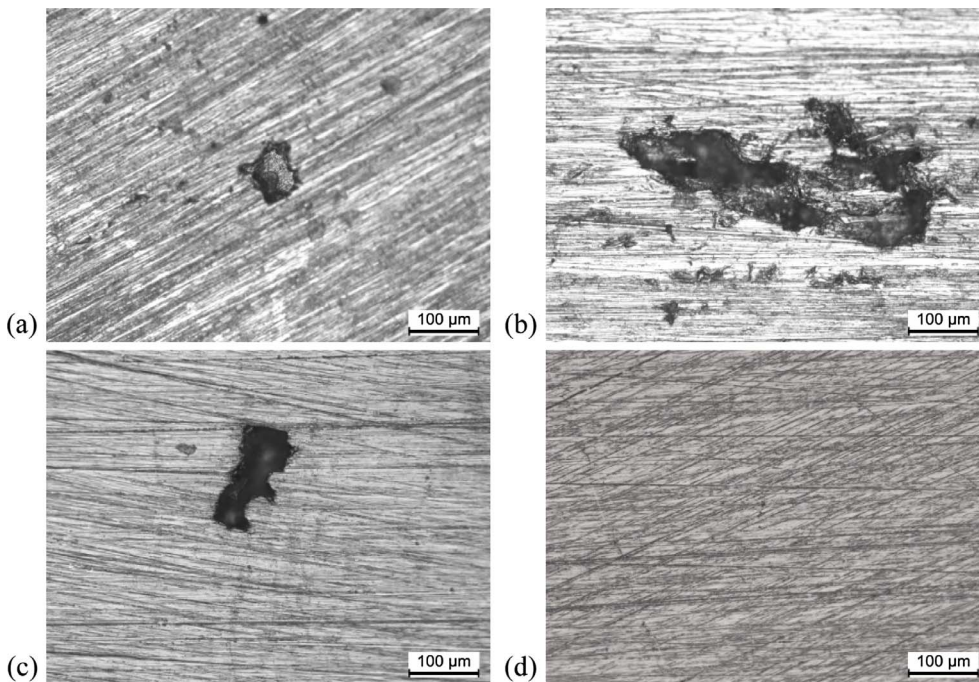
Fig. 11. The micrographs of the dissected cubes from the sample (a) region No. 1, (b) region No. 2, (c) region No. 3, (d) region No. 4.

nondestructive and destructive measurement results agreed well, which showed that the present method can effectively detect the flaws of 316L stainless steel sample fabricated by SLM using the conventional ultrasonic C-scan system and common frequencies. As a matter of fact, we regard all the signals between the front-wall and back-wall as the structural noise, and we define the anomalous and excessive noise as 'flaw echo' based on statistical theory. Compared with the traditional fixed threshold method, both false positives and missed detection are effectively suppressed. In addition, the fixed threshold used in the traditional C-scan method is usually determined by the inspectors artificially rather than using the automatic algorithm; however, the present method is automatic. Future work will be focused on the extreme value statistics of the non-Gaussian backscattering data.

Acknowledgements

Appendix A. Supplementary material

Supplementary data associated with this article can be found, in the online version, at http://dx.doi.org/10.1016/j.measurement.2018.01. 020.

References

[1] H. Rieder, M. Spies, J. Bamberg, B. Henkel, On-and offline ultrasonic characterization of components built by SLM additive manufacturing, in: D.E. Chimenti, L.J. Bond (Eds.), Review Progress QNDE, Vol. 1706 AIP Publishing, 2016, p. 130002.

[2] N.P. Aleshin, M.V. Grigor'ev, N.A. Shchipakov, M.A. Prilutskii, V.V. Murashov, Applying nondestructive testing to quality control of additive manufactured parts, Russ. J. Nondestr. Test. 52 (2016) 600–609.

[3] D. Lévesque, C. Bescond, M. Lord, X. Cao, P. Wanjara, J.P. Monchalin, Inspection of additive manufactured parts using laser ultrasonics, in: D.E. Chimenti, L.J. Bond

(Eds.), Rev. Prog. QNDE, Vol. 1706 AIP Publishing, 2016, p. 130003.

[4] B. Fay, K. Brendel, G. Ludwig, Studies of inhomogeneous substances by ultrasonic back-scattering, Ulrasound. Med. Biol. 2 (1976) 195–198.

[5] C.M. Kube, J.A. Turner, Voigt, Reuss, Hill, and self-consistent techniques for modeling ultrasonic scattering, in: D.E. Chimenti, L.J. Bond (Eds.), Review of Progress in QNDE, Vol. 1650 AIP Publishing, 2015, pp. 926–934.

[6] L. Yu, R.B. Thompson, F.J. Margetan, The spatial correlation of backscattered ultrasonic grain noise: theory and experimental validation, IEEE. T. Ultrason. Ferr. 57 (2010) 363–378.

[7] O.I. Lobkis, L. Yang, J. Li, S.I. Rokhlin, Ultrasonic backscattering in polycrystals with elongated single phase and duplex microstructures, Ultrasonics 52 (2012) 694–705.

[8] J.H. Rose, Ultrasonic backscatter from microstructure, in: D.O. Thompson, D.E. Chimenti (Eds.), Rev Prog QNDE, Vol. 11 1993, pp. 1677–1684.

[9] Y.K. Han, R.B. Thompson, Ultrasonic backscattering in duplex microstructures: theory and application to titanium alloys, Metall. Mater. Trans. A. 28 (1997) 91–104.

[10] G. Ghoshal, J.A. Turner, R.L. Weaver, Wigner distribution of a transducer beam pattern within a multiple scattering formalism for heterogeneous solids, J. Acoust. Soc. Am. 122 (2007) 2009–2021.

[11] Y. Song, C.M. Kube, J.A. Turner, X. Li, Statistics associated with the scattering of ultrasound from microstructure, Ultrasonics. 80 (2017) 58–61.

[12] G. Ghoshal, J.A. Turner, Diffuse ultrasonic backscatter at normal incidence through a curved interface, J. Acoust. Soc. Am. 128 (2010) 3449–3458.

[13] E. Castillo, Extreme value theory in engineering, Academic Press, London, 1988.

[14] B.J. Engle, F.J. Margetan, L.J. Bond, Relationship between near-surface ultrasonic shear-wave backscatter and grain size in metals, in: D.E. Chimenti, L.J. Bond (Eds.), Rev Prog QNDE, Vol. 1706 AIP Publishing, 2016, p. 130004.

[15] F.J. Margetan, I. Yalda, R.B. Thompson, Predicting gated-peak grain noise distributions for ultrasonic inspections of metals, in: D.O. Thompson, D.E. Chimenti (Eds.), Rev Prog QNDE, Vol. 15 Plenum, 1996, pp. 1509–1516.

[16] M. Ni, C. Chen, X. Wang, P. Wang, R. Li, X. Zhang, K. Zhou, Anisotropic tensile behavior of in situ precipitation strengthened Inconel 718 fabricated by additive manufacturing, Mater. Sci. Eng. A. 701 (2017) 344–351.

[17] X. Li, Y. Song, F. Liu, H. Hu, P. Ni, Evaluation of mean grain size using the multi-scale ultrasonic attenuation coefficient, NDT&E. Int. 72 (2015) 25–32.

[18] R. Osserman, The isoperimetric inequality, B. Am. Math. Soc. 84 (1978) 1182–1238.

[19] V.L. de Araújo Freitas, V.H.C. de Albuquerque, E. de Macedo Silva, A.A. Silva, J.M.R. Tavares, Nondestructive characterization of microstructures and determination of elastic properties in plain carbon steel using ultrasonic measurements, Mater. Sci. Eng. A. 527 (2010) 4431–4437.

[20] J.A. Cherry, H.M. Davies, S. Mehmood, N.P. Lavery, S.G.R. Brown, J. Sienz, Investigation into the effect of process parameters on microstructural and physical properties of 316L stainless steel parts by selective laser melting, Int. J. Adv. Manuf. Technol. 76 (2015) 869–879.

[21] N.V. Karthik, H. Gu, D. Pal, T. Starr, B. Stucker, High frequency ultrasonic non destructive evaluation of additively manufactured components, In 24th International Solid Freeform Fabrication Symposium, 2013, pp. 311–325.